Macromolecules

pubs.acs.org/Macromolecules Article

Topological Design and Mechanical Manipulation of Matrix-Free Polymer Grafted Nanoparticles Driven by Bond Exchanging

Qionghai Chen, Wanhui Huang, Liqun Zhang, Venkat Ganesan, and Jun Liu*

Cite This: *Macromolecules* 2024, 57, 10474−10486 Read Online

ACCESS | Metrics & More | Article Recommendations | Supporting Information

ABSTRACT: Tailoring mechanical properties through bond exchange reactions (BERs) demands precise topological manipulation, yet accurately correlating structures and properties to complex topologies remains a challenge. This investigation delves into matrix-free polymer grafted nanoparticles (PGNPs) with dynamic covalent bonds and examines how topological control can modulate material properties. Through coarse−grained molecular dynamics simulations, the alterations in the grafted polymer uniformity (α) induced by BERs triggered by terminals of grafted polymers are examined. Innovative α-kinetics theoretical model is proposed to capture the temporal evolution of topologies and elucidate the significant influence of BER kinetics and initial topology. Additionally, the α-equilibrium theoretical model characterizes equilibrium topologies, revealing the geometric distribution of grafted polymers. The theoretical models are further extended to include scenarios beyond terminal-triggered BERs, affirming their comprehensive applicability. Subsequently, it is elucidated how specific topological configurations can significantly enhance toughness and reveal the intrinsic mechanisms, which enable the construction of structure−property relationships. In summary, this study not only addresses the experimental challenges in the topological characterization of PGNPs, but also underscores the importance of strategic topological design in determining material properties and advancing material science.

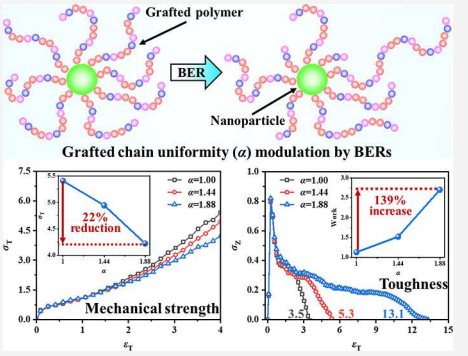

1. INTRODUCTION

Incorporating inorganic nanoparticles (NPs) into polymers typically enhances mechanical strength, optical properties, and thermal conductivity when compared to pure polymers.[1−3] The hydrophilic nature of most inorganic NPs and the nonpolar characteristics of polymers often result in mutual incompatibility within organic matrices, leading to a negative impact on material properties.[4] A widely used approach to ensure good NP dispersion is to graft polymers onto the surface of NPs.[5−7] This not only achieves uniform dispersion of NPs but also enables such materials to exhibit a range of unique properties, including improved transport of light gases,[8−10] ion transport,[11,12] phononic and photonic band gap properties,[13] and enhanced impact resistance.[14,15]

The properties of polymer grafted nanoparticles (PGNPs) are significantly influenced by numerous factors, including shape and size of the nanocore,[16] polymer chain length,[17] grafting density,[18] and number distribution of grafted polymer chains.[19] The polydispersity of grafted chain lengths is also especially crucial in influencing the properties; however, existing studies have primarily focused on systems with uniform or bimodal chain distributions.[20−22] For instance, non-cross-linked systems derive material toughness primarily from long-chain entanglement,[23] while electromagnetic applications, necessitating high filler concentrations, benefit from enhanced dispersion facilitated by short-grafted chains.[24] Further, the varied distributions of long and short chains, coupled with the multidisperse design of grafted chains, lead to diverse self-assembly behaviors.[25−27] Depending on the grafting density and polymer length, NPs can self-assemble into various structures such as strings, sheets, or globular forms.[28,29] In a recent study, Wang et al. demonstrated that mixtures of short C16 ligands and long PEG chains can lead to diverse 2D assembly morphologies of silver nanocubes at the air−water interface, highlighting the significant role that polymer length combinations play in determining the assembly behavior and morphology of NP systems.[30] For anisotropic particles, polymer grafts can control the relative orientation of NPs within their assemblies.[31] However, the limited research on the influence of polydispersity of grafted chains on the material properties hampers the understanding and utilization of its benefits, emphasizing the necessity for in-depth investigation into the polydispersity of grafted chains.

The concept of topological isomerizable network is used to describe distribution changes of branches in the polymer network, which introduces a novel perspective for exploring

Received: August 3, 2024
Revised: October 2, 2024
Accepted: October 16, 2024
Published: October 23, 2024

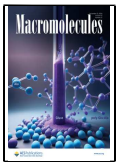

https://doi.org/10.1021/acs.macromol.4c01849
Macromolecules 2024, 57, 10474−10486

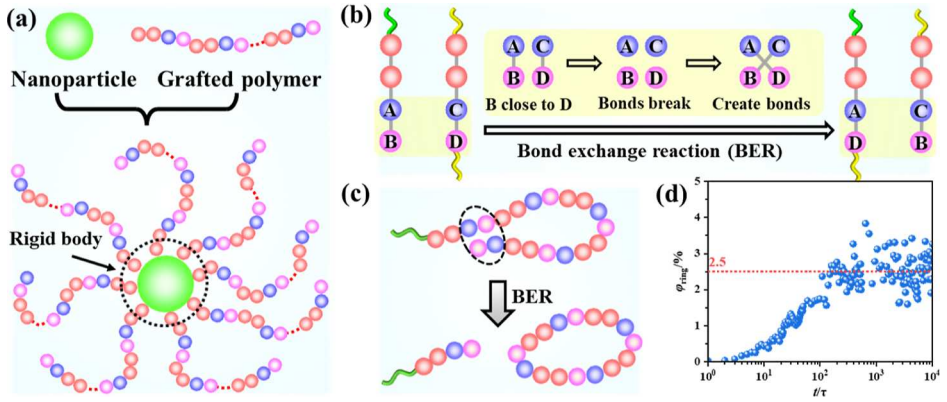

Figure 1. Model and BER algorithm. Schematic diagrams of (a) the PGNP model and (b) the BER process. (c) The outcome of the BER within a single grafted polymer. (d) Percentage of ring polymer as a function of BER time.

the polydispersity of grafted chains in PGNPs.[32] This method not only modulates the polydispersity of grafted chains through bond exchange reactions (BERs) but also enables further customization of the grafted polymer post-molding. However, the complexity of PGNP presents significant challenges in accurately characterizing the polydispersity of the polymer chains, making it challenging to establish structure−property relationships. To tackle these challenges, molecular dynamics simulations provide a robust method for analyzing material structures and establishing structure−property relationships,[33−35] while theoretical validation based on simulation results offers insights into the influence of structures on properties.[36]

In this study, we focus on the process of topological isomerization (referring to polydispersity change of the grafted chains) of PGNP and its impact on mechanical properties. To effectively control and delve deeper into the topological structures, we employed coarse−grained molecular dynamics simulations[37,38] (CGMD) and BER algorithm.[39,40] Based on simulation results and theoretical derivations, we established theoretical models that accurately capture changes and equilibrium states of these topological structures. Moreover, by precisely manipulating topologies and conducting simulations of mechanical properties, we elucidated the mechanisms by which topological structures influence mechanical performance. Our study proposes a new research paradigm for manipulating the topological structures of PGNPs and for developing structure−property relationships.

2. MODELS AND METHODOLOGIES

2.1. Model Construction. We utilize CGMD simulations to study matrix-free PGNPs. An experimental example involves grafted polyisoprene chains onto the surface of silica,[41] with the substitution of polyisoprene chains with molecular chains such as polycaprolactone capable of undergoing BERs.[32] In the described model, NPs are characterized by a radius of R_{NP} = 2.0σ, while the radius of each grafted polymer bead is set at R_p = 0.5σ, as illustrated in Figure 1a. Each system is composed of n_n = 27 NPs, with each NP grafted with n_g = 20 grafted polymers, and each grafted polymer consisting n_p = 44 beads. To inhibit the movement of directly bonded grafted polymer beads on the NP surface, these beads, along with the NP, are considered a single rigid body (as demarcated by the beads within a black dotted circle in Figure 1a). As depicted in Figure 1a, each set of four beads constitutes a unit, with each unit possessing a dynamic bond linking the blue beads to the purple beads. This setup allows for a directed BER consistent with the experiment.[32] Notably, the initial unit of the grafted polymer (directly attached to the NP) functions as the grafted site, remaining stationary and unaffected by BERs. The subsequent units, capable of transferring between grafted polymers via BERs, are termed grafted units. There are $n = n_n n_g$ grafted sites and $m = n(n_p/4 - 1)$ grafted units in the systems. More details on model construction process are available in Supporting Information Section S1.

Unlike the approach that employs the three-body potential to implement the BER process,[42] we use the commands fix/react in LAMMPS to implement the BER.[40] The BER is triggered from the termini of the grafted polymer, as illustrated in Figure 1b. When the purple bead B at the terminus of the grafted polymer encounters with the purple bead D in the middle of the grafted polymer, the A−B and C−D bonds break with a thermodynamic probability P_{sw}, while A−D and C−B bonds are simultaneously formed. BERs are influenced by several factors, including catalyst type, catalyst concentration, and reaction temperature.[43,44] Catalysts play a crucial role in reducing the activation energy required for BERs, while temperature provides the necessary energy for the reaction to proceed.[45] In simulations, these experimental conditions are emulated by adjusting the activation energy ΔE_{sw} and temperature T, with P_{sw} being governed by $P_{sw} = \exp[-\Delta E_{sw}/(k_B T)]$, where k_B is the Boltzmann constant. If a BER occurs between two separate grafted polymers (Figure 1b), two new grafted polymers are produced. The content of ring polymers comprises only approximately 2.5% with the occurrence of BERs, as depicted in Figure 1d. Differences in the chemistry between the NPs and the polymer beads do not change the content of ring polymers at equilibrium (Figure S2). To streamline subsequent theoretical derivations, BERs that result in ring molecules are excluded from simulations. Furthermore, the BERs occur not only between grafted chains on the same NP but also between grafted chains on different NPs.

BERs induce changes in the topology, consequently altering the distribution of the grafted polymer. To quantitatively characterize this transition, similar to the concept of the polydispersity index, we introduce the parameter α to assess the uniformity of the grafted polymer

$$\alpha = \frac{\sum_{i=0}^{i=m} P_i(i+1)^2}{[\sum_{i=0}^{i=m} P_i(i+1)]^2} \quad (1)$$

https://doi.org/10.1021/acs.macromol.4c01849
Macromolecules 2024, 57, 10474−10486

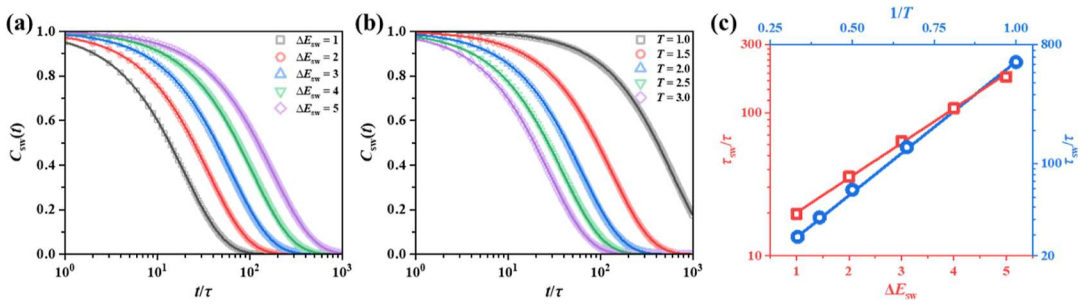

Figure 2. BER kinetics. The time dependence of the bond autocorrelation function $C_{sw}(t)$ at various (a) activation energy ΔE_{sw} under $T = 2.0$ and (b) temperatures T under $\Delta E_{sw} = 3$. (c) The BER lifetime τ_{sw} for different ΔE_{sw} and T systems. Each $C_{sw}(t)$ curve is fitted with the KWW equation, represented by the solid line.

where i represents the number of grafted units and 1 denotes the unit of the grafted site. $P_i = n_i/n$ represents the ratio of grafted chains with i grafted units, where n_i is the number of grafted chains with i grafted units.

2.2. Molecular Dynamics Simulation. In our simulations, we characterize all nonbonded interactions using the expanded truncated and shifted Lennard-Jones (L-J) potential,[46] expressed as follows

$$U_{ij}(r) = \begin{cases} 4\varepsilon_{ij}\left[\left(\frac{\sigma}{r-\Delta_{ij}}\right)^{12} - \left(\frac{\sigma}{r-\Delta_{ij}}\right)^{6}\right] - C, & 0 < r-\Delta_{ij} < r_{cutoff} \\ 0, & r-\Delta_{ij} \geq r_{cutoff} \end{cases} \quad (2)$$

where $U_{ij}(r)$ denotes the interaction potential between particles i and j at distance r. The term ε_{ij} represents the strength of interaction between the particles, while constant C is introduced to maintain the continuity of the potential energy at the cutoff distance r_{cutoff}, beyond which the potential energy is set to zero. The parameter Δ_{ij} accounts for the excluded volume between particles i and j, and it ensures that the potential energy is properly calculated based on the physical separation between the particles. By utilizing dimensionless L-J units, with ε and σ serving as the respective units, we generalize our analysis to encompass a class of polymers rather than focusing on specific molecular structures. The ε_{ij} is set to 1ε, while the r_{cutoff} is fixed at 2.24σ for simulating weakly attractive polymer systems.

The stretching energy between adjacent beads is represented by the harmonic potential[47]

$$U_{stretch}(l) = k_{stretch}(l - l_0)^2 \quad (3)$$

where $k_{stretch}$ denotes the stiffness constant for bond stretching, and l_0 represents the equilibrium bond length. For all systems, the parameters $k_{stretch}$ and l_0 standardized to $100\varepsilon/\sigma^2$ and 1σ, respectively.

The Nosé–Hoover temperature thermostat and pressure barostat are employed for equilibration within the NPT ensemble (constant number of particles N, pressure P, and temperature T). The movement of all beads is governed by the equations of motion, which are integrated using the velocity-Verlet algorithm with a time step of 0.001τ. After finalizing the model construction (Supporting Information Section S1), each system underwent a simulation for 10000τ at $T = 1$ and pressure $P = 1$, and the structures resulting from these simulations were leveraged for subsequent analysis.

2.3. Uniaxial Tensile Deformation. To explore mechanical strength, we conduct uniaxial tensile deformation in nonequilibrium MD simulations, a widely adopted method for such investigations.[48,49] The simulation box undergoes deformation along the Z-direction at a constant engineering strain rate $\dot{\varepsilon}_T$, while the lengths in the X and Y directions adjust proportionally to maintain constant volume. The $\dot{\varepsilon}_T$ is defined as the change in length along the Z-direction over time t, normalized by the initial length $L_Z(0)$. It is set to $0.0327/\tau$ in this study.[50,51] The tensile stress σ_T is calculated using the formula[52]

$$\sigma_T = (-3P_{ZZ} + \sum_i P_{ii})/2 \quad (4)$$

where P_{ZZ} represents the pressure in the Z-direction, $\sum_i P_{ii}$ denotes the sum of pressures in all three directions. Furthermore, we utilize the second-order Legendre polynomial to quantify the orientation degree of polymer chains, expressed as

$$\langle P_2(\cos\theta)\rangle = (3\langle\cos^2\theta\rangle - 1)/2 \quad (5)$$

Here, θ denotes the angle between the given bond's direction and the deformation axis, and $\langle\cdots\rangle$ signifies ensemble averaging. The value of $\langle P_2(\cos\theta)\rangle$ ranges from -0.5 to 1, with extremes representing perfect orientation perpendicular or parallel to the deformation direction, and 0 indicating random orientation.

2.4. Triaxial Tensile Deformation. To investigate toughness, we perform triaxial tensile deformation in NEMD simulations to obtain stress–strain ($\sigma_Z - \varepsilon_T$) curves, a method proven effective in prior studies.[53,54] In these simulations, deformation occurs exclusively along the Z-axis, while the lengths in the X and Y directions remain constant, in contrast to the method where the stresses are equalized in the three principal directions.[55] The $\dot{\varepsilon}_T$ is also set to $0.0327/\tau$.[51] It is noteworthy that the stress considered here is the σ_Z, representing the stress in the Z-axis direction, distinct from the σ_T used in uniaxial tensile deformation. The toughness is represented by the area enclosed by the $\sigma_Z - \varepsilon_T$ curve. This approach enables a qualitative comparison of toughness among different systems.

We conducted CGMD simulations using the LAMMPS software developed by Sandia National Laboratories.[56] Visual-

https://doi.org/10.1021/acs.macromol.4c01849
Macromolecules 2024, 57, 10474–10486

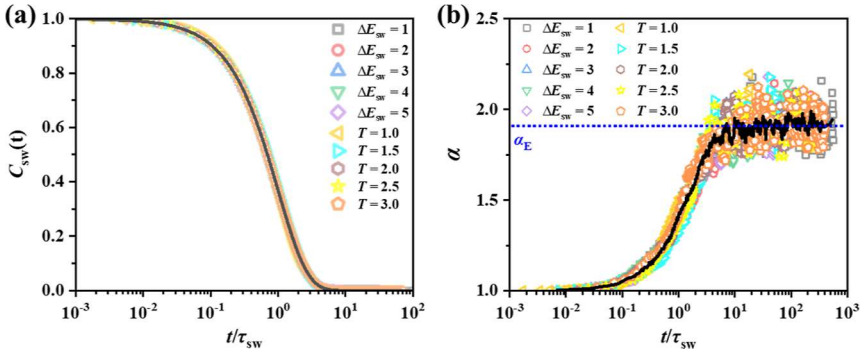

Figure 3. The time−temperature-activation energy superposition principle (TTASP). (a) Bond autocorrelation functions $C_{sw}(t)$ after scaling the time by τ_{sw} for different ΔE_{sw} systems with $T = 2$ and different T systems with $\Delta E_{sw} = 3$. The solid line represents the master curve of $C_{sw}(t)$. (b) Variation of α with time for different ΔE_{sw} and T systems after scaling times with τ_{sw}. The solid line depicts the statistical average of α for all ΔE_{sw} and T systems.

ization of the simulation processes was performed using Ovito software.[57]

3. RESULTS AND DISCUSSIONS

3.1. Kinetics of BER and α. To conduct a quantitative analysis of topological kinetics, it is imperative to comprehend the dynamical behavior of BER. We achieve this by examining the normalized bond autocorrelation function, denoted as $C_{sw}(t)$

$$C_{sw}(t) = \langle \overline{N_b(t_0 + t) \bullet N_b(t_0)} \rangle \quad (6)$$

where $N_b(t_0)$ represents the number of dynamic bonds at the time t_0, and $N_b(t_0 + t)$ represents how many of these dynamic bonds are left at the time $t_0 + t$. It should be emphasized that $N_b(t_0 + t)$ does not include those dynamic bonds that have already participated in reactions. For example, if dynamic bonds A−B and C−D undergo a BER and become A−D and B−C at time t_0 to $t_0 + t$, $N_b(t_0 + t)$ does not include A−D and B−C. In eq 6, $C_{sw}(t) = \langle \overline{N_b(t_0 + t) \bullet N_b(t_0)} \rangle$, the angular brackets $\langle \cdots \rangle$ represent an average over multiple initial times t_0, while the overbar denotes normalization. Specifically, normalization is done using $\langle N_b(t_0)\, N_b(t_0) \rangle$.Figure 2a,b illustrate the time dependence of $C_{sw}(t)$ for different systems with varying values of ΔE_{sw} and T, respectively, demonstrating that lower values of ΔE_{sw} and higher T lead to a more rapid decay of $C_{sw}(t)$. The $C_{sw}(t)$ exhibits an exponential decay, which can be effectively described by the Kohlrausch−Williams−Watts (KWW) equation $C_{sw}(t) = \exp[-(t/\tau_{sw})^{\beta}]$, where τ_{sw} represents the BER lifetime and $\beta = 1$ indicates a first-order kinetics for the BER.[58,59] The τ_{sw} for various ΔE_{sw} and T systems are shown in Figure 2c, which aligns with the Arrhenius equation $\tau_{sw} = \tau_0 \exp[\Delta E_{sw}/(k_B T)]$, where τ_0 is the pre-factor related to diffusion kinetics and $\exp[\Delta E_{sw}/(k_B T)]$ is the inverse of thermodynamic reaction probability P_{sw}. The results depicted in Figure 3c indicate a decrease in τ_{sw} with decreasing ΔE_{sw} and increasing T. The BER rate k_{sw} can be expressed as $k_{sw} = k_0 P_{sw}$, representing the occurrence of BERs per unit time, where $k_0 = n_g/\tau_0$. This observation suggests an intuitive acceleration of the BER by decreasing ΔE_{sw} and increasing T (Figure S3).

The time−temperature superposition principle, extensively utilized in polymer kinetics analysis, assumes consistent temperature dependence across different normal modes of polymer chains.[60,61] To validate its applicability to BER kinetics, we scale BER times with τ_{sw}. In Figure 3a, the $C_{sw}(t)$ curves, scaled by τ_{sw} for various ΔE_{sw} and T systems, collectively fit into a master curve $C_{sw}(t) = \exp[-(t/\tau_{sw})]$, confirming BER's compliance with the TTASP. BER alters the number of grafted units in the grafted polymer, consequently affecting α. Upon analyzing the BER time dependence of α, we find that TTASP also applies to α kinetics. Figure 3b demonstrates this applicability, where the variations of α with time for all ΔE_{sw} and T systems conform to a master curve after scaling the time by τ_{sw} (solid line in Figure 3b). Initially, α increases with the BER time, eventually converging to α_E, which represents the uniformity of grafted polymer at BER equilibrium. Additionally, variations in ΔE_{sw} and T exclusively impact the increase rate of α and do not alter α_E. The smaller the τ_{sw}, or in other words, the greater the k_{sw}, the greater the change rate of α (Figure S4). In systems with varying grafted densities and stiffness of the grafted polymer, α exhibits a consistent pattern of change, suggesting that this trend is not coincidental (Figure S5). Furthermore, the study of the proportion of BERs between grafted chains on different NPs reveals that these reactions predominantly occur between grafted chains on different NPs, accounting for approximately 76% (Figure S6). Additionally, decreasing the grafting density and increasing the stiffness of the grafted chains enhance the BERs between the grafted chains on different NPs (Figure S6d,e).

The application of TTASP to BER and α kinetics suggests that catalysts or increased temperature can accelerate BERs, facilitating rapid control of topology structures.[62−64] By scaling time with the τ_{sw}, the time axis becomes dimensionless. Experimentally, by measuring the τ_{sw}, we can similarly scale the time and obtain the corresponding master curve shown in Figure 3b. In other words, once the τ_{sw} is measured experimentally, it can be used in conjunction with the master curve in Figure 3b to accurately adjust the reaction time to achieve the desired α.

3.2. Theoretical Calculation of α. Figure 3b showcases the kinetics variation curve for α concerning monodisperse grafted polymers, but its utility for guiding experimental work is constrained. The primary limitation stems from the fact that grafted polymers in experiments are usually polydisperse, making the existing kinetics curves less relevant. Additionally, pinpointing the determinants of α_E presents a significant challenge. To overcome these hurdles, there is a need for the formulation of theoretical models that can shed light on the kinetics of α.

https://doi.org/10.1021/acs.macromol.4c01849
Macromolecules 2024, 57, 10474−10486

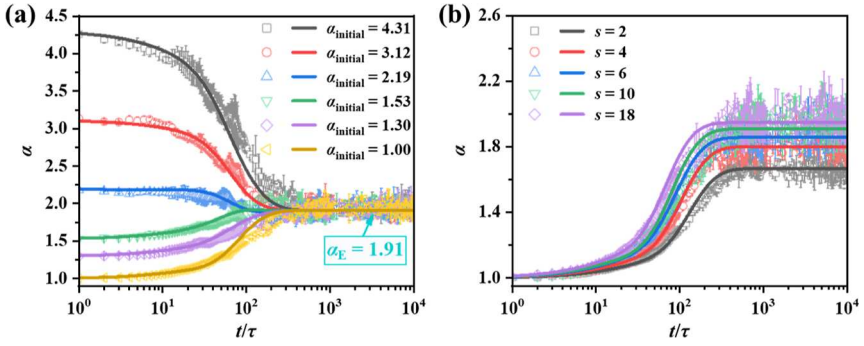

Figure 4. Theoretical calculation of α-kinetics. α as a function of BER time for different (a) initial topologies $\alpha_{initial}$ and (b) mean quantity of grafted units s. The scatter symbols are the results obtained from the simulations and the solid lines are the results from the theoretical model. The simulations are repeated three times for each variable to plot the error bars.

For a system with n grafted sites and m grafted units, the mean quantity of grafted units is represented by $s = m/n$. To elucidate the uniformity of the grafted polymer, we initially deduce the probability of the grafted polymer with i-grafted units at time t, symbolized as $P_i(t)$. Presuming each BER within the system to be random and given that $m,n \gg 1$, the change rate of grafted polymer with i-grafted units ($i > 0$) at time t can be articulated as

$$\frac{dP_i}{dt} = \sum_{j=0}^{j=i-1} k_{sw}(w_{i>j}^{j\to i}P_j - w_{i>j}^{i\to j}P_i) + \sum_{j=i+1}^{j=m} k_{sw}(w_{i<j}^{j\to i}P_j - w_{i<j}^{i\to j}P_i) \quad (7)$$

where $w_{i>j}^{j\to i}$ denotes the probability of conversion from a grafted polymer with j-grafted units to one with i-grafted units, for cases where i is greater than j. For conversions that increase grafted polymers with i-grafted units, $w_{i>j}^{j\to i} = \sum_{k=i-j}^{k=m} P_k/m$ and $w_{i<j}^{j\to i} = 1/m$. Conversely, for conversions leading to a decrease in grafted polymers with i-grafted units, $w_{i>j}^{i\to j} = 1/m$ and $w_{i<j}^{i\to j} = \sum_{k=j-i}^{k=m} P_k/m$. By inserting the expressions for the K_{sw} and the conversion probabilities into eq 7, we obtain the following derivation

$$P_i(t) = [P_i(0) - F_i]e^{-E_i t} + F_i \quad (8)$$

where $F_i = [1 - \sum_{j=0}^{j=i-1}\sum_{l=0}^{l=i-j-1} P_l(t)P_j(t)]/(i + s + 1)$ and $E_i = (i + s + 1)/(s\tau_{sw})$. Specifically, $F_0 = 1/(1 + s)$ and $E_i = (s + 1)/(s\tau_{sw})$. More details of the theoretical model derivation are given in Supporting Information Section S3. It is important to emphasize that our theoretical model is a mean field model, which assumes that all bonding sites are equally accessible. This simplification makes the theoretical framework more manageable but may overlook specific spatial constraints. For instance, bonding sites near the NP surface or those surrounded by grafted chains of different lengths may have varying levels of accessibility. Furthermore, NPs of low curvature may lead to less accessible bonds versus those with high curvature. Future work could incorporate these spatial considerations to provide a more accurate representation of the system.

By integrating the definition of α (eq 1), the theoretical model for α-kinetics can be articulated as follows

$$\alpha(t) = \frac{\sum_{i=0}^{i=m} P_i(t)(i+1)^2}{(s+1)^2} \quad (9)$$

The theoretical model of α-kinetics demonstrates that α-kinetics are influenced exclusively by the τ_{sw}, $P_i(0)$, and s. The significance of τ_{sw} on α-kinetics has been verified in Figures 3b and S4. To further validate the influence of the initial topology $\alpha_{initial}$ on α-kinetics, we set $s = 10$ and examined α-kinetics across various $\alpha_{initial}$, as showcased in Figure 4a. The α values for systems with differing $\alpha_{initial}$ tend to converge toward α_E with the progression of BER time. The theoretical predictions for α-kinetics (represented by solid lines in Figure 4a) are in close agreement with the simulation outcomes, accurately depicting the evolution of α-kinetics and validating that α_E = 1.91 when $s = 10$. Figure 4b presents both simulation and theoretical findings regarding α-kinetics for systems with varied s, indicating that α_E ascends with an increase in s. Moreover, as s increases leading to a larger k_{sw} (Figure S7), the rate at which α changes also accelerates with the increase in s. Furthermore, we observed that α increased with increasing s, after the BER reached equilibrium (α reached stabilization).

Traditionally, the manipulation of grafted polymer topologies has been guided by empirical adjustments of BER durations within experimental frameworks.[32,65] This approach requires intermittent cessation of the reaction to conduct structural assessments, significantly extending the duration of experimental procedures. Moreover, the intricacies involved in evaluating the molecular weight distribution of polymers grafted onto NPs, as opposed to linear polymers, complicates the establishment of definitive structure−property correlations. The theoretical model we introduce for α-kinetics sheds light on precise reaction time management, thereby mitigating these challenges and enhancing the precision in achieving targeted α values.

We recognize that eq 9 does not yield an analytical solution. However, as $t \to \infty$ and BER equilibrium is attained, the possibility emerges for deriving an analytical solution to facilitate more in-depth analysis. To advance a more detailed examination and more intuitively unravel the quantitative interplay between α_E and s, it is imperative to develop the theoretical model for α-equilibrium further. Equation 8 delineates that the equilibrium probability of the grafted polymer with i-unit (P_{i_E}) can be articulated as

https://doi.org/10.1021/acs.macromol.4c01849
Macromolecules 2024, 57, 10474−10486

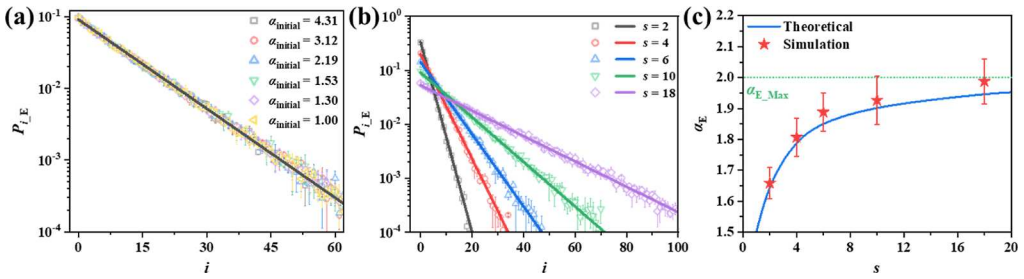

Figure 5. Theoretical calculation of α-equilibrium. The distribution of grafted polymer at equilibrium for different (a) initial topologies $\alpha_{initial}$ and (b) mean quantity of grafted units s. (c) α at equilibrium as a function of the mean quantity of grafted units s. All scatter symbols are the results obtained from the simulation and all solid lines are the results from the theoretical model. The simulations are repeated three times for each variable to plot the error bars.

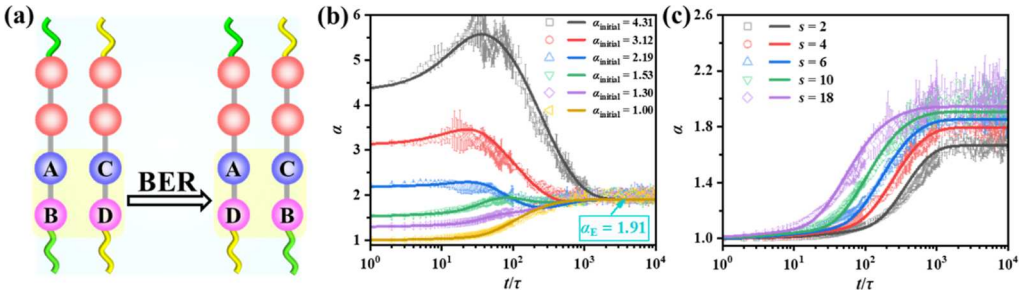

Figure 6. Theoretical calculation of α-kinetics for free BER. (a) Schematic diagrams of newly introduced BER process. α as a function of BER time for different (b) $\alpha_{initial}$ models and (c) the number of grafted units of the grafted polymer. The BER rate for systems with $\alpha_{initial}$ less than 2 is adjusted by an empirical correction factor $\xi = 1 + s/20$ (Supporting Information Section S2). The scatter symbols are the results obtained from the simulation and the solid lines are the results from the theoretical model. The simulations are repeated three times for each variable to plot the error bars.

$$P_{i\_E} = \begin{cases} \dfrac{1}{s+1}, & i = 0 \\ \dfrac{1 - \sum_{j=0}^{j=i-1} \sum_{l=0}^{l=i-j-1} P_{l\_E} P_{j\_E}}{i+s+1}, & i > 0 \end{cases} \tag{10}$$

Utilizing the principle of mathematical induction,[66] it can be demonstrated that

$$P_{i\_E} = \frac{1}{s+1}\left(1 - \frac{1}{s+1}\right)^i \tag{11}$$

Equation 11 illustrates the equilibrium geometric distribution of grafted polymers, which is dependent exclusively on the s. Systems with varied $\alpha_{initial}$ converge to the same equilibrium distribution of grafted polymers when s is consistent, as depicted in Figure 5a. In contrast, systems with different values of s, result in unique equilibrium geometric distributions of grafted polymers, as shown in Figure 5b.

Drawing from the grafted polymer's geometric distribution, with its expected value $E_i = s$ and variance $\mathrm{Var}_i = s + s^2$, we deduce

$$\alpha_E = \frac{\mathrm{Var}(i) + E^2(i) + 2\mathrm{E}(i) + 1}{(s+1)^2} = \frac{2s+1}{s+1} \tag{12}$$

Equation 12 shows that α_E is only affected by s. Figure 5c presents the theoretical model of α-equilibrium (represented by the solid line), which aligns closely with the simulation data across different s systems (indicated by scatter symbols). Additionally, by applying eq 12, the maximal uniformity of the grafted polymer at equilibrium, α_{E_MAx}, is derived as $\lim_{s\to\infty} \alpha_E = 2$, as illustrated in Figure 5c.

The integration of simulation outcomes with theoretical model predictions provides compelling evidence for the geometric distribution pattern of polymers grafted onto NPs. This finding diverges from conventional polymerization theories that typically predict exponential or Gaussian distributions for the molecular weight profiles of polymers.[67] Our α-equilibrium theoretical model posits that leveraging dynamic covalent bonding in grafted polymers paves the way for the facile synthesis of polymers characterized by geometrically distributed branching.

3.3. Extend the α Theoretical Calculation to Free BER.

In previous discussions, BER was characterized as being triggered by dynamic bonds at the termini of grafted polymers, necessitating the involvement of terminal dynamic bonds. The concept of "free BER" breaks through this limitation, allowing dynamic bonds at any position along the grafted polymer chain, not just the terminals, to initiate BERs. This indicates that internal dynamic bonds within the polymer chain can also trigger reactions, thereby moving beyond the constraint of requiring terminal dynamic bonds to participate. This new perspective offers a more flexible approach to understanding and controlling the structural characteristics of PGNPs, particularly in terms of the length distribution of grafted chains.

Specifically, the free BER introduces a novel BER type into the system, as depicted in Figure 6a. When the purple bead B in the middle of the grafted polymer encounters the purple bead D in the middle of another grafted polymer, the A−B and C−D bonds break with a probability of P_{sw}, while A−D and C−B bonds form concurrently.

We similarly derive a theoretical model of α-kinetics based on eq 7. Due to the change in the BER mode, the conversion

https://doi.org/10.1021/acs.macromol.4c01849
Macromolecules 2024, 57, 10474−10486

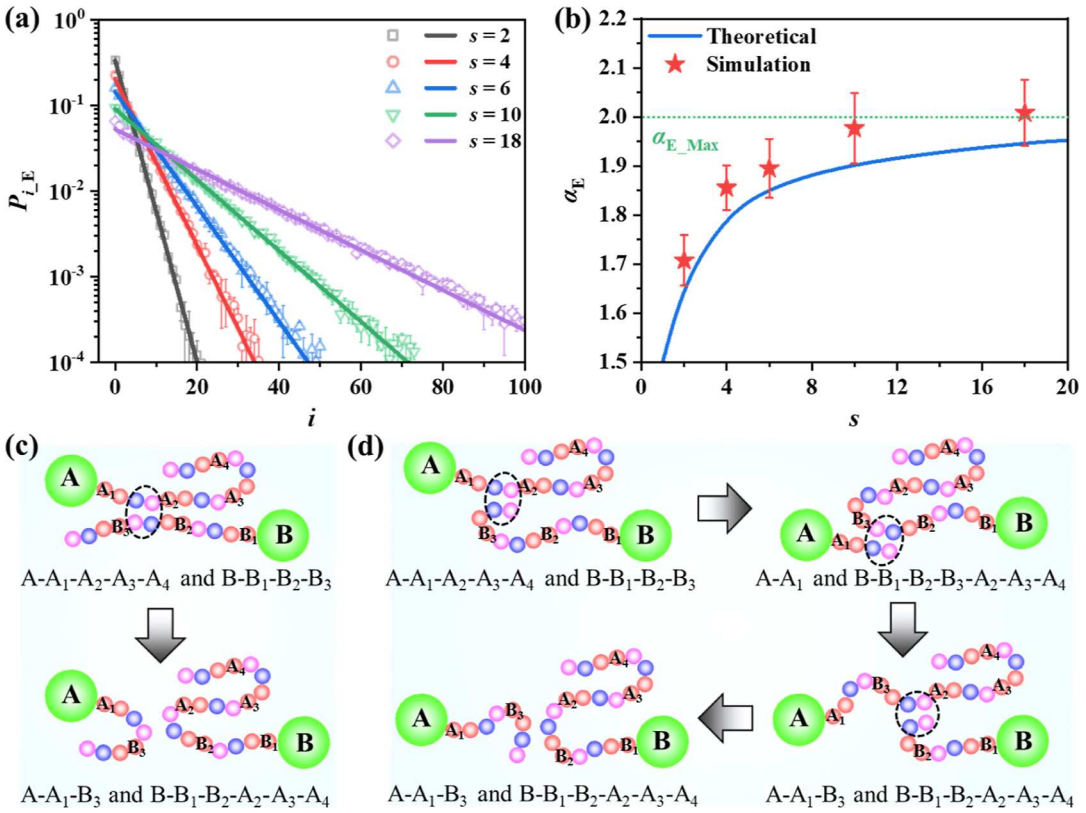

Figure 7. Theoretical calculation of α-equilibrium for free BER between grafted polymers. (a) The distribution of grafted polymer at equilibrium for different mean quantity of grafted units s. (b) α at equilibrium as a function of the mean quantity of grafted units s. Schematic diagram of the structural changes after (c) free BER between grafted polymers and (d) BERs triggered by the termini of the grafted polymer. All scatter symbols are the results obtained from the simulation and the solid lines are the results from the theoretical model. The simulations are repeated three times for each variable to plot the error bars.

probabilities also differ. For conversions that lead to an increase in the number of grafted polymers with i-grafted units, the conversion probabilities are given by

$$w'^{j\to i}_{i>j} = \frac{n}{m^2}\left[\sum_{l=i-j}^{l=i}(l-i+j+1)P_{i-j} + \sum_{l=i+1}^{l=m}(j+1)P_l\right]$$

and

$$w'^{j\to i}_{i<j} = \frac{n}{m^2}\left[\sum_{l=0}^{l=i-1}(l+1)P_l + \sum_{l=i}^{l=m}(i+1)P_l\right]$$

For conversions that result in a decrease in the number of grafted polymers with i-grafted units, the conversion probabilities are

$$w'^{i\to j}_{i>j} = \frac{n}{m^2}\left[\sum_{l=0}^{l=j}(l+1)P_l + (j+1)\sum_{l=j+1}^{l=m}P_l\right]$$

and

$$w'^{i\to j}_{i<j} = \frac{n}{m^2}\left[\sum_{l=1}^{l=i} lP_{l+j-i+1} + (i+1)\sum_{l=j}^{l=m}P_l\right]$$

By incorporating these conversion probabilities into eq 7, we derive an expression analogous to eq 8

$$P_i(t) = [P_i(0) - F']e^{-E'_i t} + F'_i \tag{13}$$

where

$$F'_i = \left[\left(1 - \sum_{l=0}^{l=i-1}P_l(t)\right)\left(i+1+\sum_{l=0}^{l=i-1}(2l-i+1)P_l(t)\right) + \sum_{j=1}^{j=i-1}\sum_{l=i-j}^{l=i-1}(l-i+j+1)P_l(t)P_j(t)\right] \Big/ [(i+1)(s+1)]$$

and $E'_i = \frac{(i+1)(s+1)}{s\tau_{sw}}$. Specifically, $F'_0 = \frac{1}{1+s}$ and $E'_0 = \frac{s+1}{s\tau_{sw}}$.

The outcomes from both simulation and theoretical model, illustrating the temporal evolution of α for various systems characterized by $\alpha_{initial}$ and s, are showcased in Figures 6a,b. The consistency between the theoretical predictions and simulation data underscores the model's validity. Mirroring the pattern observed in the BER mode triggered by the termini of grafted polymers, α in the free BER mode also tends to stabilize at the same α_E over time. Notably, in the scenario of free BER mode where the system starts with an $\alpha_{initial}$ greater than 2, there's an initial increase in α followed by a decrease, eventually steadying at α_E.

Owing to the intricate nature of F'_i, formulating a theoretical model of α-equilibrium through mathematical induction poses significant difficulties. As an alternative, we initially adopted the principle of detailed balance. At equilibrium, the transformation between grafted polymers complies with the detailed balance conditions within the realm of thermodynamic equilibrium

$$P_{i\_E}w^{i\to i+1} = P_{i+1\_E}w^{i+1\to i} \tag{14}$$

https://doi.org/10.1021/acs.macromol.4c01849
Macromolecules 2024, 57, 10474−10486

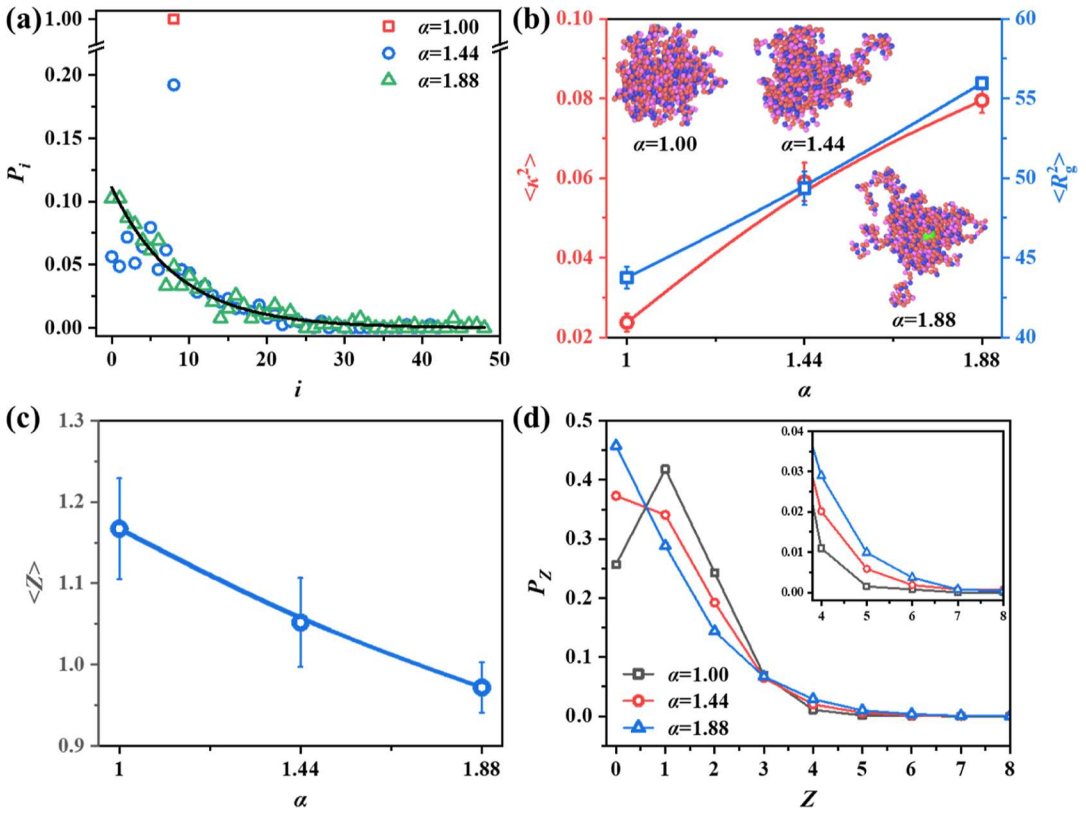

Figure 8. Structural characterization. The (a) distributions of grafted polymer, (b) average asphericity $\langle\kappa^2\rangle$ and squared radius of gyration $\langle R_g^2\rangle$ of PGNPs, (c) average number of entanglements of grafted polymer and (d) entanglement number distribution for different α systems.

where P_{i_E} and P_{i+1_E} denote the probabilities of grafted polymer with i-grafted units and $(i + 1)$-grafted units, respectively. The conversion probability from a grafted polymer with i-grafted units to one with $(i + 1)$-grafted units is given by $w^{i\to i+1} = \frac{n[\sum_{j=0}^{j=i} jP_{j\_E} + (i+1)\sum_{j=i+1}^{j=m} P_{j\_E}]}{m^2}$, and the reverse conversion probability, from a grafted polymer with $(i + 1)$-grafted units to one with i-grafted units, is $w^{i+1\to i} = \frac{n[\sum_{j=0}^{j=i}(j+1)P_{j\_E} + (i+1)\sum_{j=i+1}^{j=m} P_{j\_E}]}{m^2}$. By substituting these conversion probabilities into eq 14, the following expression can be derived

$$\frac{P_{i+1\_E}}{P_{i\_E}} = 1 - \frac{\sum_{j=0}^{j=i} P_{j\_E}}{1 + \sum_{j=0}^{j=i} jP_{j\_E} + i[1 - \sum_{j=0}^{j=i} P_{j\_E}]} \quad (15)$$

Integrating mathematical induction with eq 15 enables the derivation of a formula that mirrors the distribution pattern of grafted polymers as outlined in eq 11. Consequently, the α-equilibrium theoretical model for the free BER model aligns precisely with the model triggered at the termini of grafted polymers, as encapsulated in eq 12.

Figure 7a,b showcase the outcomes of both the theoretical model and simulations for P_{i_E} and α_E under the scenario of free BER among grafted polymers, validating the efficacy of our equilibrium theoretical model. These results confirm that the mode of BER exerts no impact on the equilibrium topology of grafted polymers. It is reasonable to anticipate that the equilibrium topology of grafted polymers remains unaffected by the specific BER mode employed. For every structure realized through a free BER, as illustrated in Figure 7c, an equivalent structure can be achieved via three termini-triggered BERs, as depicted in Figure 7d. In Figure 7c, NPs A and B are grafted with polymer chains $A_1-A_2-A_3-A_4$ and $B_1-B_2-B_3$, denoted as $A-A_1-A_2-A_3-A_4$ and $B-B_1-B_2-B_3$, respectively. Following a free BER event, the resulting structures are $A-A_1-B_3$ and $B-B_1-B_2-A_2-A_3-A_4$. Figure 7d illustrates that starting from $A-A_1-A_2-A_3-A_4$ and $B-B_1-B_2-B_3$, after three termini-initiated BERs, the structures $A-A_1-B_3$ and $B-B_1-B_2-A_2-A_3-A_4$ can be similarly generated. Although the pathways differ, both BER modes can yield identical grafted polymer structures (including the sequence of unit connections), indicating that BER modes may influence α-kinetics but not the α-equilibrium state.

3.4. Mechanical Properties. To pave the way for understanding the influence of topology on mechanical properties, we initiate our discussion by examining the structural characteristics of PGNPs across different α values. Unlike Phukan et al.'s work on the mechanical response of NP networks,[68] our focus is on the influence of α on mechanical properties, without allowing cross-linking between the end of grafted chains to form a network structure.

Beginning with a system with α = 1.00 as the foundational structure, we employ BERs to derive two distinct systems characterized by α = 1.44 and α = 1.88. These configurations symbolize homogeneous, transitional, and equilibrium topologies, respectively, with the distribution patterns of the grafted polymers depicted in Figure 8a. Notably, the system with α = 1.88 exhibits an approximate geometric distribution of grafted polymers, as illustrated by the black solid line in Figure 8a. NPs within the three distinct topological structures are well-dispersed throughout the system, without any occurrence of aggregation (Figure S8). Subsequently, we

https://doi.org/10.1021/acs.macromol.4c01849
Macromolecules 2024, 57, 10474−10486

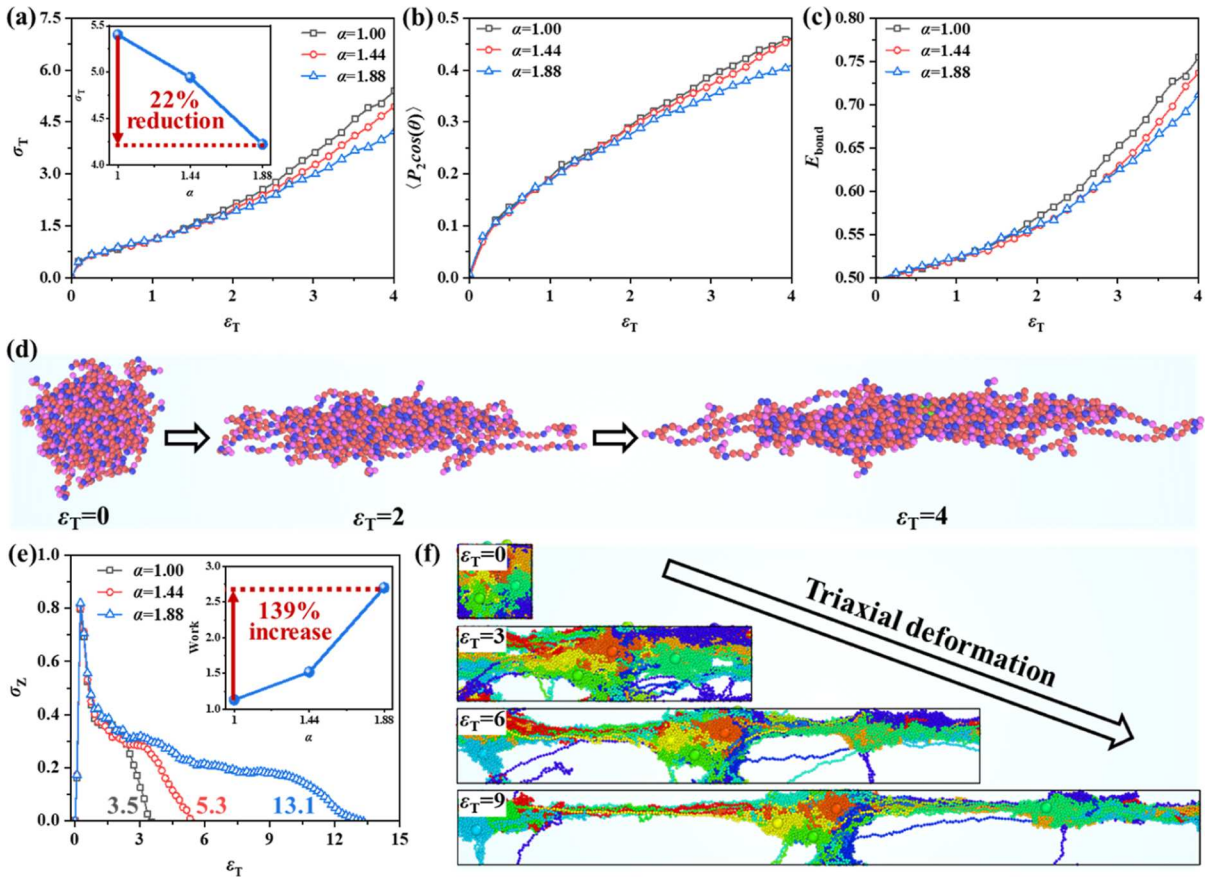

Figure 9. Mechanical properties. (a) Uniaxial tensile stress, (b) bond orientation and (c) bond energy as a function of strain for different alpha systems. (d) Snapshots of individual PGNP in uniaxial deformation at different strains for the system with α = 1.00. (e) Triaxial tensile stress as a function of strain for different alpha systems. (f) Snapshots of the system with α = 1.88 at different strains in triaxial deformation. Different colors represent different PGNPs.

commenced our investigation into the anisotropy of PGNPs by computing the gyration tensor for each NP and extracting its three eigenvalues λ_1, λ_2, and λ_3, organized in descending order as $\lambda_1 \geq \lambda_2 \geq \lambda_3$. The aggregate of these eigenvalues equates to the squared radius of gyration, $R_g^2 = \lambda_1 + \lambda_2 + \lambda_3$. For anisotropy quantification, we introduce the asphericity κ^2 of PGNPs, defined as $\kappa^2 = \frac{3}{2}\frac{\lambda_1^2 + \lambda_2^2 + \lambda_3^2}{(\lambda_1 + \lambda_2 + \lambda_3)^2} - \frac{1}{2}$.[69−71] The asphericity κ^2 spans from 0 to 1, where $\kappa^2 = 0$ symbolizes an isotropic shape of PGNPs, depicting a spherical symmetrical distribution of all atoms, and $\kappa^2 = 1$ signifies a highly anisotropic shape, with atoms aligned linearly. This parameter sheds light on the shapes of PGNPs across different distributions of grafted polymers. Figure 8b showcases the mean asphericity $\langle\kappa^2\rangle$ and squared radius of gyration $\langle R_g^2\rangle$ across diverse α configurations, illustrating that heightened α values correspond to increases in both $\langle\kappa^2\rangle$ and $\langle R_g^2\rangle$, indicative of the enhanced heterogeneity in PGNPs. This observation is bolstered by snapshots of individual PGNPs within varied α systems, as depicted in the inset of Figure 8b, where the increase in α is associated with the presence of longer grafted polymers alongside shorter ones, contributing to the PGNPs' augmented heterogeneity.

The Z1+ algorithm[72,73] serves to compute the average entanglement number $\langle Z\rangle$ across varying α systems, as shown in Figure 8c. These findings reveal a relationship between α and $\langle Z\rangle$, where a lower α is associated with a higher $\langle Z\rangle$. The distribution of the entanglement number, P_Z (where Z represents the entanglement number), is further detailed in Figure 8d. In the system characterized by α = 1.88, which has a higher proportion of shorter grafted polymers as depicted in Figure 8a, there's a noticeable increase in the number of grafted polymers with Z = 0. Conversely, the system with α = 1.00 shows a greater occurrence of grafted polymers with Z < 3, yet a reduction in those with Z > 3. Although longer-grafted polymers contribute to a higher Z, their presence in the system is relatively minimal. Hence, it is deduced that systems with elevated α values typically exhibit a higher Z.

Having conducted a detailed analysis of structural characteristics, we now turn our attention to the exploration of mechanical properties to gain a deeper understanding of how different topologies specifically influence performance. Initially, we assessed the mechanical strength of various α systems through uniaxial deformation, with the corresponding stress−strain ($\sigma_T - \varepsilon_T$) curves illustrated in Figure 9a. Notably, at ε_T = 4, the mechanical strength of the α = 1.88 system saw a 22% reduction in comparison to the α = 1.00 system, as shown in the inset of Figure 9a. This decrease is largely due to the higher entanglement number present in the α = 1.00 system, as evidenced in Figure 8c. To delve deeper into why the α = 1.00 system exhibits superior mechanical strength, we analyzed the bond orientation degree $\langle P_2(\cos\theta)\rangle$ and bond energy E_{bond}, both of which significantly influence the system's stress. The alignment of bond orientation with the deformation direction amplifies the force component in that direction, and a heightened E_{bond} signifies an increased force acting on the

https://doi.org/10.1021/acs.macromol.4c01849
Macromolecules 2024, 57, 10474−10486

bond. The variations of $\langle P_2(\cos\theta)\rangle$ and E_{bond} with ε_T across different α systems are depicted in Figures 9b,c, respectively. Owing to its higher entanglement number, the α = 1.00 system demonstrates enhanced $\langle P_2(\cos\theta)\rangle$ and E_{bond} values, contributing to its optimal mechanical strength. Figure 9d offers snapshots of individual PGNPs at varying ε_T, providing insight into the microstructural alterations during uniaxial deformation. The entanglement of grafted polymers across different NPs facilitates their alignment in the deformation direction, bolstering mechanical strength.

After analyzing the mechanical strength of the systems, we further explore the critical property of toughness to comprehensively assess the impact of different topologies on mechanical behavior. We employed triaxial deformation[53,54] to investigate the toughness of various α systems, with the corresponding stress–strain ($\sigma_Z - \varepsilon_T$) curves presented in Figure 9e. This deformation method induces void formation within the system, with the number of voids escalating as strain increases. To facilitate the comparison of the $\sigma_T - \varepsilon_T$ curves for triaxial and uniaxial deformation, we also give the $\sigma_T - \varepsilon_T$ curves during triaxial deformation, as shown in Figure S9. A system's toughness is determined by its ability to withstand void formation without fracturing. For instance, the breaking strain for the α = 1.00 system was measured at 3.5, whereas for the α = 1.88 system, it notably increased to 13.1. To quantitatively assess the toughness across different α systems, we integrated the area under the $\sigma_Z - \varepsilon_T$ curves, with the findings illustrated in the inset of Figure 9e. Remarkably, the toughness of the α = 1.88 system surged by 139% in comparison to the α = 1.00 system. This variance in toughness is ascribed to the distinct distributions of grafted polymers and their $\langle Z\rangle$. In the α = 1.00 system, despite a high $\langle Z\rangle$, the system predominantly comprises grafted polymers with Z of 1 and 2. This configuration facilitates the disentanglement of grafted polymers on different NPs under triaxial stress, resulting in a reduced breaking strain. As α escalates, there's an uptick in some longer grafted polymers, consequently increasing the prevalence of grafted polymers with $Z > 3$, as depicted in Figure 8d. This proliferation of Z among longer grafted polymers enables the system, especially at α = 1.88, to maintain a cohesive physical entanglement network under significant strains, effectively enhancing its structural integrity and preventing breakage. The α = 1.88 system, with its abundance of longer grafted polymers, achieves a 274.2% enhancement in breaking strain and a 139% uplift in toughness relative to the α = 1.00 system, as illustrated in Figure 9e. The dispersity-toughness relationships here are in general agreement with studies that looked at bidisperse star systems.[74] For a more illustrative depiction of the toughness enhancement and breaking strain mechanisms, Figure 9f showcases snapshots of the α = 1.88 system under varying strains. Different colors are assigned to PGNPs to facilitate the observation of entanglements across diverse NPs. The interlacing of long grafted polymers forms numerous "thin stems", typically consisting of grafted polymers in varied colors, indicating their formation through the entanglement of graft polymers on disparate NPs. These "thin stems" bridge various NPs, ensuring the system retains a cohesive physical network that forestalls breakage.

4. CONCLUSIONS

Our research aims to investigate the impact of BERs on the topology of grafted polymers and establish a clear correlation between structure and properties. Initially, we verified that both the BER kinetics and the evolution of grafted polymer topology adhere to the time-activation energy–temperature superposition principle. This enabled us to construct dynamic master curves for BERs and the topology of grafted polymers. Within these dynamic master curves, we observed an increase in the α with the duration of BER time, ultimately stabilizing at α_E determined by s. Building on these observations, we proposed a precise theoretical model of α-kinetics to describe these dynamic changes, offering valuable insights into determining the optimal reaction cessation time required to achieve the desired topology. Additionally, we developed a theoretical model of α-equilibrium, illustrating that the distribution of grafted polymers adopts a geometric pattern at equilibrium, solely influenced by s. Extending our theoretical models to the free BER mode, we compared the theoretical models of α-kinetics and α-equilibrium for both BER modes. Despite differences in α-kinetics theoretical model, the α-equilibrium theoretical models for both BER modes are consistent. Notably, our findings reveal that mechanical properties can be finely tuned through topological control. Systems with uniformly distributed grafted polymers exhibit enhanced mechanical strength due to a higher entanglement number, while systems with exponentially distributed grafted polymers demonstrate greater toughness owing to the presence of longer grafted chains.

In conclusion, our developed theoretical models precisely characterize the topology of grafted polymers and establish a clear correlation between topology and mechanical properties. This connection holds considerable potential for applications in areas like flexible electronics[75] and soft robotics,[76,77] substantially broadening the utility of PGNP systems in various advanced technological domains.

■ ASSOCIATED CONTENT

Supporting Information

The Supporting Information is available free of charge at https://pubs.acs.org/doi/10.1021/acs.macromol.4c01849.

Model construction process; the adjustment of BER rate for free BER mode; the dynamic theoretical derivation of α (PDF)

■ AUTHOR INFORMATION

Corresponding Author

Jun Liu − *State Key Laboratory of Organic–Inorganic Composites, College of Materials Science and Engineering, Beijing University of Chemical Technology, Beijing 100029, People's Republic of China;* orcid.org/0000-0001-7369-1875; Email: liujun@mail.buct.edu.cn

Authors

Qionghai Chen − *State Key Laboratory of Organic–Inorganic Composites, College of Materials Science and Engineering, Beijing University of Chemical Technology, Beijing 100029, People's Republic of China*

Wanhui Huang − *State Key Laboratory of Organic–Inorganic Composites, College of Materials Science and Engineering, Beijing University of Chemical Technology, Beijing 100029, People's Republic of China*

Liqun Zhang − *State Key Laboratory of Organic−Inorganic Composites, College of Materials Science and Engineering, Beijing University of Chemical Technology, Beijing 100029, People's Republic of China;* orcid.org/0000-0002-2103-6294

Venkat Ganesan − *Department of Chemical Engineering, The University of Texas at Austin, Austin, Texas 78712, United States;* orcid.org/0000-0003-3899-5843

Complete contact information is available at: https://pubs.acs.org/10.1021/acs.macromol.4c01849

Notes

The authors declare no competing financial interest.

■ ACKNOWLEDGMENTS

J.L. acknowledges the National Science Fund for Excellent Young Scholars (52122311) and the National Natural Science Foundation of China (52373222). V.G. acknowledges partial support from Welch Foundation (F-1599), and to the donors of the American Chemical Society Petroleum Research Fund (66812-ND7).

■ REFERENCES

(1) Kumar, S. K.; Jouault, N.; Benicewicz, B.; Neely, T. Nanocomposites with Polymer Grafted Nanoparticles. *Macromolecules* **2013**, *46*, 3199−3214.

(2) Hui, C. M.; Pietrasik, J.; Schmitt, M.; Mahoney, C.; Choi, J.; Bockstaller, M. R.; Matyjaszewski, K. Surface-Initiated Polymerization as an Enabling Tool for Multifunctional (Nano-)Engineered Hybrid Materials. *Chem. Mater.* **2014**, *26*, 745−762.

(3) Kumar, S. K.; Benicewicz, B. C.; Vaia, R. A.; Winey, K. I. 50th Anniversary Perspective: Are Polymer Nanocomposites Practical for Applications? *Macromolecules* **2017**, *50*, 714−731.

(4) Fröhlich, J.; Niedermeier, W.; Luginsland, H.-D. The Effect of Filler−Filler and Filler−Elastomer Interaction on Rubber Reinforcement. *Compos. Part A Appl. Sci. Manuf.* **2005**, *36*, 449−460.

(5) Akcora, P.; Liu, H.; Kumar, S. K.; Moll, J.; Li, Y.; Benicewicz, B. C.; Schadler, L. S.; Acehan, D.; Panagiotopoulos, A. Z.; Pryamitsyn, V.; Ganesan, V.; Ilavsky, J.; Thiyagarajan, P.; Colby, R. H.; Douglas, J. F. Anisotropic Self-Assembly of Spherical Polymer-Grafted Nanoparticles. *Nat. Mater.* **2009**, *8*, 354−359.

(6) Kubiak, J. M.; Li, B.; Suazo, M.; Macfarlane, R. J. Polymer Grafted Nanoparticle Composites with Enhanced Thermal and Mechanical Properties. *ACS Appl. Mater. Interfaces* **2022**, *14*, 21535−21543.

(7) Ogane, S.; Sato, R.; Tanaka, Y.; Tsutsui, K.; Moriguchi, K. (Digital Presentation) Development of an Eam-Type Interatomic Potential Model Reproducing Theoretical Energetics in Polytype Structures. *ECS Meet. Abstr.* **2022**, *MA2022−01*, 2286.

(8) Bilchak, C. R.; Buenning, E.; Asai, M.; Zhang, K.; Durning, C. J.; Kumar, S. K.; Huang, Y.; Benicewicz, B. C.; Gidley, D. W.; Cheng, S.; Sokolov, A. P.; Minelli, M.; Doghieri, F. Polymer-Grafted Nanoparticle Membranes with Controllable Free Volume. *Macromolecules* **2017**, *50*, 7111−7120.

(9) Bilchak, C. R.; Jhalaria, M.; Huang, Y.; Abbas, Z.; Midya, J.; Benedetti, F. M.; Parisi, D.; Egger, W.; Dickmann, M.; Minelli, M.; Doghieri, F.; Nikoubashman, A.; Durning, C. J.; Vlassopoulos, D.; Jestin, J.; Smith, Z. P.; Benicewicz, B. C.; Rubinstein, M.; Leibler, L.; Kumar, S. K. Tuning Selectivities in Gas Separation Membranes Based on Polymer-Grafted Nanoparticles. *ACS Nano* **2020**, *14*, 17174−17183.

(10) Jeong, S. P.; Kumar, R.; Genix, A.-C.; Popov, I.; Li, C.; Mahurin, S. M.; Hu, X.; Bras, W.; Popovs, I.; Sokolov, A. P.; Bocharova, V. Improving Gas Selectivity in Membranes Using Polymer-Grafted Silica Nanoparticles. *ACS Appl. Nano Mater.* **2021**, *4*, 5895−5903.

(11) Choudhury, S.; Stalin, S.; Deng, Y.; Archer, L. A. Soft Colloidal Glasses as Solid-State Electrolytes. *Chem. Mater.* **2018**, *30*, 5996−6004.

(12) Srivastava, S.; Schaefer, J. L.; Yang, Z.; Tu, Z.; Archer, L. A. 25th Anniversary Article: Polymer−Particle Composites: Phase Stability and Applications in Electrochemical Energy Storage. *Adv. Mater.* **2014**, *26*, 201−234.

(13) Alonso-Redondo, E.; Schmitt, M.; Urbach, Z.; Hui, C. M.; Sainidou, R.; Rembert, P.; Matyjaszewski, K.; Bockstaller, M. R.; Fytas, G. A New Class of Tunable Hypersonic Phononic Crystals Based on Polymer-Tethered Colloids. *Nat. Commun.* **2015**, *6*, 8309.

(14) Hyon, J.; Gonzales, M.; Streit, J. K.; Fried, O.; Lawal, O.; Jiao, Y.; Drummy, L. F.; Thomas, E. L.; Vaia, R. A. Projectile Impact Shock-Induced Deformation of One-Component Polymer Nanocomposite Thin Films. *ACS Nano* **2021**, *15*, 2439−2446.

(15) Chen, S. H.; Souna, A. J.; Stranick, S. J.; Jhalaria, M.; Kumar, S. K.; Soles, C. L.; Chan, E. P. Controlling Toughness of Polymer-Grafted Nanoparticle Composites for Impact Mitigation. *Soft Matter* **2022**, *18*, 256−261.

(16) Frischknecht, A. L.; Hore, M. J. A.; Ford, J.; Composto, R. J. Dispersion of Polymer-Grafted Nanorods in Homopolymer Films: Theory and Experiment. *Macromolecules* **2013**, *46*, 2856−2869.

(17) Jhalaria, M.; Buenning, E.; Huang, Y.; Tyagi, M.; Zorn, R.; Zamponi, M.; García-Sakai, V.; Jestin, J.; Benicewicz, B. C.; Kumar, S. K. Accelerated Local Dynamics in Matrix-Free Polymer Grafted Nanoparticles. *Phys. Rev. Lett.* **2019**, *123*, 158003.

(18) Tawade, B. V.; Singh, M.; Apata, I. E.; Veerasamy, J.; Pradhan, N.; Karim, A.; Douglas, J. F.; Raghavan, D. Polymer-Grafted Nanoparticles with Variable Grafting Densities for High Energy Density Polymeric Nanocomposite Dielectric Capacitors. *JACS Au* **2023**, *3*, 1365−1375.

(19) Liu, H.; Zhao, H.-Y.; Müller-Plathe, F.; Qian, H.-J.; Sun, Z.-Y.; Lu, Z.-Y. Distribution of the Number of Polymer Chains Grafted on Nanoparticles Fabricated by Grafting-to and Grafting-from Procedures. *Macromolecules* **2018**, *51*, 3758−3766.

(20) Martin, T. B.; Jayaraman, A. Identifying the Ideal Characteristics of the Grafted Polymer Chain Length Distribution for Maximizing Dispersion of Polymer Grafted Nanoparticles in a Polymer Matrix. *Macromolecules* **2013**, *46*, 9144−9150.

(21) Shi, R.; Qian, H.-J.; Lu, Z.-Y. Computer Simulation Study on the Self-Assembly of Unimodal and Bimodal Polymer-Grafted Nanoparticles in a Polymer Melt. *Phys. Chem. Chem. Phys.* **2017**, *19*, 16524−16532.

(22) Midya, J.; Rubinstein, M.; Kumar, S. K.; Nikoubashman, A. Structure of Polymer-Grafted Nanoparticle Melts. *ACS Nano* **2020**, *14*, 15505−15516.

(23) Kubiak, J. M.; Macfarlane, R. J. Forming Covalent Crosslinks between Polymer-Grafted Nanoparticles as a Route to Highly Filled and Mechanically Robust Nanocomposites. *Adv. Funct. Mater.* **2019**, *29*, 1905168.

(24) Shi, R.; Qian, H.-J.; Lu, Z.-Y. Tuning Cavitation and Crazing in Polymer Nanocomposite Glasses Containing Bimodal Grafted Nanoparticles at the Nanoparticle/Polymer Interface. *Phys. Chem. Chem. Phys.* **2019**, *21*, 7115−7126.

(25) Rungta, A.; Natarajan, B.; Neely, T.; Dukes, D.; Schadler, L. S.; Benicewicz, B. C. Grafting Bimodal Polymer Brushes on Nanoparticles Using Controlled Radical Polymerization. *Macromolecules* **2012**, *45*, 9303−9311.

(26) Michalek, L.; Mundsinger, K.; Barner-Kowollik, C.; Barner, L. The Long and the Short of Polymer Grafting. *Polym. Chem.* **2019**, *10*, 54−59.

(27) Xing, J.-Y.; Lu, Z.-Y.; Liu, H.; Xue, Y.-H. The Selectivity of Nanoparticles for Polydispersed Ligand Chains during the Grafting-to Process: A Computer Simulation Study. *Phys. Chem. Chem. Phys.* **2018**, *20*, 2066−2074.

(28) Akcora, P.; Liu, H.; Kumar, S. K.; Moll, J.; Li, Y.; Benicewicz, B. C.; Schadler, L. S.; Acehan, D.; Panagiotopoulos, A. Z.; Pryamitsyn, V.; Ganesan, V.; Ilavsky, J.; Thiyagarajan, P.; Colby, R. H.; Douglas, J.

F. Anisotropic Self-Assembly of Spherical Polymer-Grafted Nanoparticles. *Nat. Mater.* **2009**, *8*, 354−359.
(29) Zhou, Y.; Bore, S. L.; Tao, A. R.; Paesani, F.; Arya, G. Many-Body Potential for Simulating the Self-Assembly of Polymer-Grafted Nanoparticles in a Polymer Matrix. *npj Comput. Mater.* **2023**, *9*, 224.
(30) Wang, Y.; Zhou, Y.; Yang, Q.; Basak, R.; Xie, Y.; Le, D.; Fuqua, A. D.; Shipley, W.; Yam, Z.; Frano, A.; Arya, G.; Tao, A. R. Self-Assembly of Nanocrystal Checkerboard Patterns via Non-Specific Interactions. *Nat. Commun.* **2024**, *15*, 3913.
(31) Gao, B.; Arya, G.; Tao, A. R. Self-Orienting Nanocubes for the Assembly of Plasmonic Nanojunctions. *Nat. Nanotechnol.* **2012**, *7*, 433−437.
(32) Zou, W.; Jin, B.; Wu, Y.; Song, H.; Luo, Y.; Huang, F.; Qian, J.; Zhao, Q.; Xie, T. Light-Triggered Topological Programmability in a Dynamic Covalent Polymer Network. *Sci. Adv.* **2020**, *6*, No. eaaz2362.
(33) Ferrari, A.; Körmann, F.; Asta, M.; Neugebauer, J. Simulating Short-Range Order in Compositionally Complex Materials. *Nat. Comput. Sci.* **2023**, *3*, 221−229.
(34) Chen, Q.; Zhang, Z.; Huang, Y.; Zhao, H.; Chen, Z.; Gao, K.; Yue, T.; Zhang, L.; Liu, J. Structure−Mechanics Relation of Natural Rubber: Insights from Molecular Dynamics Simulations. *ACS Appl. Polym. Mater.* **2022**, *4*, 3575−3586.
(35) Chen, Q.; Huang, W.; Duan, P.; Yue, T.; Zhang, L.; Wu, X.; Liu, J. Manipulating the Mechanical Properties of Cis-Polyisoprene Nanocomposites via Molecular Dynamics Simulation. *Polymer* **2022**, *256*, 125233.
(36) Li, S.-J.; Shi, X. Tailoring Antifouling Properties of Nanocarriers via Entropic Collision of Polymer Grafting. *ACS Nano* **2021**, *15*, 5725−5734.
(37) Wang, S.; Huang, M.; Wu, Y.-N.; Chu, W.; Zhao, J.; Walsh, A.; Gong, X.-G.; Wei, S.-H.; Chen, S. Effective Lifetime of Non-Equilibrium Carriers in Semiconductors from Non-Adiabatic Molecular Dynamics Simulations. *Nat. Comput. Sci.* **2022**, *2*, 486−493.
(38) Batzner, S. Biasing Energy Surfaces towards the Unknown. *Nat. Comput. Sci.* **2023**, *3*, 190−191.
(39) Gissinger, J. R.; Jensen, B. D.; Wise, K. E. Modeling Chemical Reactions in Classical Molecular Dynamics Simulations. *Polymer* **2017**, *128*, 211−217.
(40) Gissinger, J. R.; Jensen, B. D.; Wise, K. E. REACTER: A Heuristic Method for Reactive Molecular Dynamics. *Macromolecules* **2020**, *53*, 9953−9961.
(41) Liu, Y.; Wang, Z.; Zhao, Y.; Hou, G.; Jiang, R.; Bockstaller, M. R.; Qin, X.; Zhang, L.; Matyjaszewski, K. SiO2-g-Polyisoprene Particle Brush Reinforced Advanced Elastomer Nanocomposites Prepared via ARGET ATRP. *Adv. Funct. Mater.* **2024**, *34*, 2315741.
(42) Ciarella, S.; Sciortino, F.; Ellenbroek, W. G. Dynamics of Vitrimers: Defects as a Highway to Stress Relaxation. *Phys. Rev. Lett.* **2018**, *121*, 058003.
(43) Schmidt, B. V. K. J.; Barner-Kowollik, C. Dynamic Macromolecular Material Design—The Versatility of Cyclodextrin-Based Host−Guest Chemistry. *Angew. Chem., Int. Ed.* **2017**, *56*, 8350−8369.
(44) Chakma, P.; Konkolewicz, D. Dynamic Covalent Bonds in Polymeric Materials. *Angew. Chem., Int. Ed.* **2019**, *58*, 9682−9695.
(45) Tangthana-umrung, K.; Poutrel, Q. A.; Gresil, M. Epoxy Homopolymerization as a Tool to Tune the Thermo-Mechanical Properties and Fracture Toughness of Vitrimers. *Macromolecules* **2021**, *54*, 8393−8406.
(46) Bennemann, C.; Paul, W.; Baschnagel, J.; Binder, K. Investigating the Influence of Different Thermodynamic Paths on the Structural Relaxation in a Glass-Forming Polymer Melt. *J. Phys.: Condens. Matter* **1999**, *11*, 2179−2192.
(47) Zhang, Z.; Fang, Y.; Chen, Q.; Duan, P.; Wu, X.; Zhang, L.; Wu, W.; Liu, J. Molecular Dynamics Simulation of the Impact of the Surface Topology of Carbon Black on the Mechanical Properties of Elastomer Nanocomposites. *Phys. Chem. Chem. Phys.* **2023**, *25*, 5602−5612.
(48) Wang, W.; Hou, G.; Zheng, Z.; Wang, L.; Liu, J.; Wu, Y.; Zhang, L.; Lyulin, A. V. Designing Polymer Nanocomposites with a Semi-Interpenetrating or Interpenetrating Network Structure: Toward Enhanced Mechanical Properties. *Phys. Chem. Chem. Phys.* **2017**, *19*, 15808−15820.
(49) Liu, J.; Zheng, Z.; Li, F.; Lei, W.; Gao, Y.; Wu, Y.; Zhang, L.; Wang, Z. L. Nanoparticle Chemically End-Linking Elastomer Network with Super-Low Hysteresis Loss for Fuel-Saving Automobile. *Nano Energy* **2016**, *28*, 87−96.
(50) Gao, J.; Weiner, J. H. Anisotropy Effects on Chain-Chain Interactions in Stretched Rubber. *Macromolecules* **1991**, *24*, 1519−1525.
(51) Gao, J.; Weiner, J. H. Simulated Polymer Melt Stress Relaxation. I. Plateau Behavior. *J. Chem. Phys.* **1995**, *103*, 1614−1620.
(52) Everaers, R. Constrained Fluctuation Theories of Rubber Elasticity: General Results and an Exactly Solvable Model. *Eur. Phys. J. B* **1998**, *4*, 341−350.
(53) He, J.; Chen, Q.; Qu, J.; Li, S.; Fu, Z.; Wei, Y.; Hu, S.; Feng, A.; Zhang, L.; Liu, J. Mechanically Robust and Self-Healing Elastomers Based on Dynamic Oxime−Carbamate Bonds: A Combined Experiment and All-Atom Simulation Study. *ACS Appl. Polym. Mater.* **2023**, *5*, 3161−3172.
(54) Fu, Z.; Chen, Q.; He, J.; Li, S.; Ming, R.; Wei, Y.; Xu, Y.; Liu, J.; Zhang, L. A Synergistic Effect of MXene/MWCNT Enables Self-Healable and Low Percolation Elastomer Sensor: A Combined Experiment and All-Atom Molecular Dynamics Simulation. *Compos. Sci. Technol.* **2023**, *242*, 110155.
(55) Wu, Z.; Pal, S.; Keten, S. Implicit Chain Particle Model for Polymer-Grafted Nanoparticles. *Macromolecules* **2023**, *56*, 3259−3271.
(56) Plimpton, S. Fast Parallel Algorithms for Short-Range Molecular Dynamics. *J. Comput. Phys.* **1995**, *117*, 1−19.
(57) Stukowski, A. Visualization and Analysis of Atomistic Simulation Data with OVITO−the Open Visualization Tool. *Model. Simul. Mater. Sci. Eng.* **2010**, *18*, 015012.
(58) Kalathi, J. T.; Kumar, S. K.; Rubinstein, M.; Grest, G. S. Rouse Mode Analysis of Chain Relaxation in Homopolymer Melts. *Macromolecules* **2014**, *47*, 6925−6931.
(59) Li, Y.; Kröger, M.; Liu, W. K. Nanoparticle Effect on the Dynamics of Polymer Chains and Their Entanglement Network. *Phys. Rev. Lett.* **2012**, *109*, 118001.
(60) Liu, J.; Cao, D.; Zhang, L.; Wang, W. Time-Temperature and Time-Concentration Superposition of Nanofilled Elastomers: A Molecular Dynamics Study. *Macromolecules* **2009**, *42*, 2831−2842.
(61) Bennemann, C.; Baschnagel, J.; Paul, W. Molecular-Dynamics Simulation of a Glassy Polymer Melt: Incoherent Scattering Function. *Eur. Phys. J. B* **1999**, *10*, 323−334.
(62) Nurlaela, E.; Shinagawa, T.; Qureshi, M.; Dhawale, D. S.; Takanabe, K. Temperature Dependence of Electrocatalytic and Photocatalytic Oxygen Evolution Reaction Rates Using NiFe Oxide. *ACS Catal.* **2016**, *6*, 1713−1722.
(63) Cheng, Z.; Yang, B.; Chen, Q.; Shen, Z.; Yuan, T. Quantitative Relationships between Molecular Parameters and Reaction Rate of Organic Chemicals in Fenton Process in Temperature Range of 15.8 °C−60 °C. *Chem. Eng. J.* **2018**, *350*, 534−540.
(64) Arcus, V. L.; Mulholland, A. J. Temperature, Dynamics, and Enzyme-Catalyzed Reaction Rates. *Annu. Rev. Biophys.* **2020**, *49*, 163−180.
(65) Miao, W.; Zou, W.; Jin, B.; Ni, C.; Zheng, N.; Zhao, Q.; Xie, T. On Demand Shape Memory Polymer via Light Regulated Topological Defects in a Dynamic Covalent Network. *Nat. Commun.* **2020**, *11*, 4257.
(66) Zeheb, E.; Hertz, D. Another Proof and a Generalization of a Theorem on N-Dimensional Stability. *Proc. IEEE* **1984**, *72*, 745−746.
(67) Whitfield, R.; Truong, N. P.; Anastasaki, A. Precise Control of Both Dispersity and Molecular Weight Distribution Shape by Polymer Blending. *Angew. Chem., Int. Ed.* **2021**, *60*, 19383−19388.
(68) Phukan, M.; Haritha, P.; Roy, T. R.; Iyer, B. V. S. Mechanical Response of Networks Formed by End-Functionalised Spherical Polymer Grafted Nanoparticles. *Soft Matter* **2022**, *18*, 8591−8604.

https://doi.org/10.1021/acs.macromol.4c01849
Macromolecules 2024, 57, 10474−10486

(69) Rudnick, J.; Gaspari, G. The Aspherity of Random Walks. *J. Phys. A. Math. Gen.* **1986**, *19*, L191−L193.
(70) Gaspari, G.; Rudnick, J.; Beldjenna, A. The Shapes of Open and Closed Random Walks: A 1/d Expansion. *J. Phys. A. Math. Gen.* **1987**, *20*, 3393−3414.
(71) Jagodzinski, O.; Eisenriegler, E.; Kremer, K. Universal Shape Properties of Open and Closed Polymer Chains: Renormalization Group Analysis and Monte Carlo Experiments. *J. Phys. I* **1992**, *2*, 2243−2279.
(72) Kröger, M. Shortest Multiple Disconnected Path for the Analysis of Entanglements in Two- and Three-Dimensional Polymeric Systems. *Comput. Phys. Commun.* **2005**, *168*, 209−232.
(73) Shanbhag, S.; Kröger, M. Primitive Path Networks Generated by Annealing and Geometrical Methods: Insights into Differences. *Macromolecules* **2007**, *40*, 2897−2903.
(74) Gürel, U.; Keten, S.; Giuntoli, A. Bidispersity Improves the Toughness and Impact Resistance of Star-Polymer Thin Films. *ACS Macro Lett.* **2024**, *13*, 302−307.
(75) Kang, J.; Son, D.; Wang, G. N.; Liu, Y.; Lopez, J.; Kim, Y.; Oh, J. Y.; Katsumata, T.; Mun, J.; Lee, Y.; Jin, L.; Tok, J. B. H.; Bao, Z. Tough and Water-Insensitive Self-Healing Elastomer for Robust Electronic Skin. *Adv. Mater.* **2018**, *30*, 1706846.
(76) Xia, Y.; Cedillo-Servin, G.; Kamien, R. D.; Yang, S. Guided Folding of Nematic Liquid Crystal Elastomer Sheets into 3D via Patterned 1D Microchannels. *Adv. Mater.* **2016**, *28*, 9637−9643.
(77) Qian, X.; Chen, Q.; Yang, Y.; Xu, Y.; Li, Z.; Wang, Z.; Wu, Y.; Wei, Y.; Ji, Y. Untethered Recyclable Tubular Actuators with Versatile Locomotion for Soft Continuum Robots. *Adv. Mater.* **2018**, *30*, 1801103.

https://doi.org/10.1021/acs.macromol.4c01849
Macromolecules 2024, 57, 10474−10486